HHS Public Access

Author manuscript

ACS Appl Mater Interfaces. Author manuscript; available in PMC 2022 June 30.

Published in final edited form as:

ACS Appl Mater Interfaces. 2021 June 30; 13(25): 29936–29948. doi:10.1021/acsami.1c06478.

Ultrasmall Molybdenum Disulfide Quantum Dots Cage Alzheimer's Amyloid Beta to Restore Membrane Fluidity

Yuhuan Li[1,2], **Huayuan Tang**[3], **Houjuan Zhu**[4], **Aleksandr Kakinen**[5], **Di Wang**[6], **Nicholas Andrikopoulos**[2], **Yunxiang Sun**[7], **Aparna Nandakumar**[2], **Eunbi Kwak**[2], **Thomas P. Davis**[2,5], **David Tai Leong**[4], **Feng Ding**[3], **Pu Chun Ke**[2,5,8]

[1]Liver Cancer Institute, Zhongshan Hospital, Key Laboratory of Carcinogenesis and Cancer Invasion, Ministry of Education, Fudan University, Shanghai, 200032, China

[2]Drug Delivery, Disposition and Dynamics, Monash Institute of Pharmaceutical Sciences, Monash University, 381 Royal Parade, Parkville, VIC 3052, Australia

[3]Department of Physics and Astronomy, Clemson University, Clemson, SC 29634, United States

[4]National University of Singapore, Department of Chemical and Biomolecular Engineering, 4 Engineering Drive 4, Singapore 117585, Singapore

[5]Australian Institute for Bioengineering and Nanotechnology, The University of Queensland, Brisbane Qld 4072, Australia

[6]School of Life Sciences, Jilin University, Changchun 130012, China

[7]School of Physical Science and Technology, Ningbo University, Ningbo 315211, China

[8]The GBA National Institute for Nanotechnology Innovation, 136 Kaiyuan Avenue, Guangzhou, 510700, China

Abstract

Corresponding Authors: David Tai Leong, cheltwd@nus.edu.sg; Feng Ding, fding@clemson.edu; Pu Chun Ke, pu-chun.ke@monash.edu.

Author contributions

PCK conceived the project. YL, HT, HZ, FD and PCK wrote the manuscript. YL and DW performed membrane fluidity and actin reorganization confocal fluorescence imaging, ROS assay and viability assay. HZ and DTL performed the synthesis and XRD and XPS characterizations of MoS_2 quantum dots. AK performed TEM and confocal imaging analysis. NA conducted FTIR analysis of MoS_2-Aβ binding. NA and AN performed membrane fluidity measurement with pre-incubated Aβ-o. YL and EK performed ThT and fluorescence colocalization assays. HT, YS and FD performed DMD computer simulations and analysis. All authors agreed on the presentation of the manuscript.

Conflict of Interest

The authors declare no conflict of interest.

Supporting Information

The Supporting Information is available free of charge on the ACS Publications website. AFM measurement for the thickness of ultrasmall MoS_2 QDs (**Figure S1**); Trypan blue staining of SH-S5Y cells exposed to Aβ-o and ultrasmall MoS_2 QDs (**Figure S2**); TEM imaging of Aβ-m, Aβ-o and Aβ-f (**Figure S3**); ThT kinetic assay for ultrasmall MoS_2 QDs (**Figure S4**); ATR-FTIR amide I band spectra and deconvolution analysis of Aβ with or without ultrasmall MoS_2 QDs (**Figure S5**); ATR-FTIR amide I band spectra and secondary structure distribution of ultrasmall MoS_2 QDs (**Figure S6**); Effects of pre-incubated Aβ-o on the fluidity of SH-SY5Y cell membranes in the presence and absence of ultrasmall MoS_2 QDs (**Figure S7**); Effects of Aβ-m, Aβ-f and ultrasmall MoS_2 QDs on membrane fluidity (**Figure S8**); Aβ-o distribution on SH-SY5Y cells in the presence and absence of ultrasmall MoS_2 QDs (**Figure S9**); Aβ-o distribution on SH-SY5Y cells treated with ultrasmall MoS_2 QDs (**Figure S10**); Actin organization in SH-SY5Y cells treated with ultrasmall MoS_2 QDs (**Figure S11**); Interactions between Aβ-f and ultrasmall MoS_2 QDs (**Figure S12**); Secondary structure distribution of Aβ species in the presence and absence of ultrasmall MoS_2 QDs (**Table S1**).

Alzheimer's disease (AD) is a major cause of dementia characterized by the overexpression of transmembrane amyloid precursor protein and its neurotoxic byproduct amyloid beta (Aβ). A small peptide of considerable hydrophobicity, Aβ is aggregation prone catalyzed by the presence of cell membrane, among other environmental factors. Accordingly, current AD mitigation strategies often take aim at breaking down the Aβ-membrane communication, yet no data is available concerning the cohesive interplay of the three key entities of cell membrane, Aβ, and its inhibitor. Using a lipophilic Laurdan dye and confocal fluorescence microscopy, we observed cell membrane perturbation and actin reorganization induced by Aβ oligomers, but not by Aβ monomers or amyloid fibrils. We further revealed recovery of membrane fluidity by ultrasmall MoS_2 quantum dots, also shown in this study as a potent inhibitor of Aβ amyloid aggregation. Using discrete molecular dynamics simulations, we uncovered the binding of MoS_2 and Aβ monomers as mediated by hydrophilic interactions between the quantum dots and the peptide N-terminus. In contrast, Aβ oligomers and fibrils were surface-coated by the ultrasmall quantum dots in distinct testudo-like, reverse protein-corona formations to prevent their further association with cell membrane and adverse effects downstream. This study offered a crucial new insight and a viable strategy for regulating the amyloid aggregation and membrane-axis of AD pathology with multifunctional nanomedicine.

Graphical Abstract

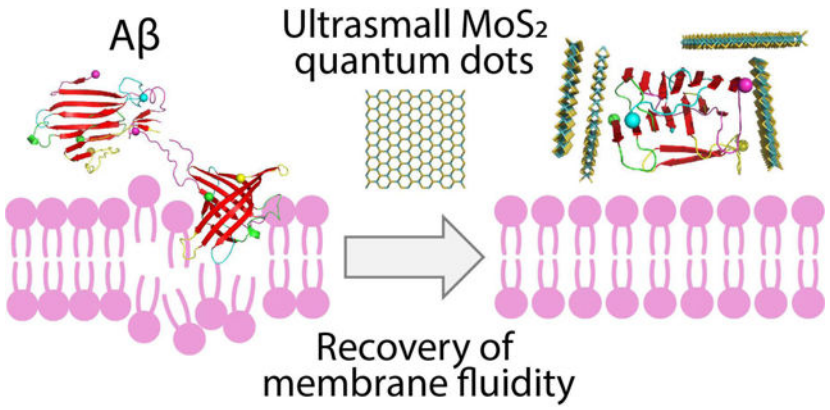

This study demonstrates an effective strategy of breaking down the membrane-axis of Alzheimer's Aβ with ultrasmall MoS_2 quantum dots. A unique "peptide core-nanoparticle corona" formation is rendered to mitigate Aβ amyloid aggregation and recover membrane fluidity.

Keywords

Aβ; MoS_2; oligomer; membrane fluidity; AD nanomedicine

1. INTRODUCTION

Alzheimer's disease (AD) is a progressive neurodegenerative disorder and a primary cause of dementia, characterized histologically by the deposition of extracellular amyloid beta (Aβ) senile plaques and intracellular hyperphosphorylated tau tangles.[1] Research over the past decades has revealed the complexity of the AD pathobiology and established the

amyloid cascade hypothesis[2] as an influential paradigm in the field implicating amyloid fibrils and, more recently, oligomers, as the most neurotoxic species of Aβ.[3, 4] Mounting laboratory and clinical evidence also supports neuroinflammation, tau accumulation and apolipoprotein E as crucial multifactorial contributors to neurodegeneration and AD pathology.[1, 5, 6]

Structurally, Aβ is synthesized from amyloid precursor protein (APP), a type-I transmembrane protein cleaved off by β and γ secretases sequentially to render the peptide isoforms. Post synthesis, Aβ is released to the extracellular space via indeterminate pathways and is present in trace amounts in central nervous system and cerebrospinal fluid.[1] This specific origin of Aβ entails its high affinity for cell membrane, and hence AD is often considered a membrane disorder.[7–10] Neurotoxicity, accordingly, is thought to be initiated by the membrane association of Aβ[11] which triggers conformational changes of the peptide and increases membrane permeability,[12, 13] coupled with interactions of the peptide with nicotinic acetylcholine receptors and cholesterol-dense lipid rafts,[14] among others. Theoretically, Aβ-membrane interaction has been described by the carpet model, the pore formation model, the membrane receptor model, as well as the detergent model.[12, 15–17] These models are derived from extensive biophysical and biochemical studies of Aβ in lipid environments, involving electrochemistry, confocal fluorescence microscopy, atomic force microscopy, nuclear magnetic resonance spectroscopy, size exclusion chromatography, immunohistochemistry, as well as molecular dynamics simulations.[17–20]

Along with the improved understanding of AD physiopathology, growing efforts over the past three decades have been devoted to the development of AD therapeutics involving the antagonists of peptidomimetics, small molecules, monoclonal antibodies and, more recently, nanomaterials.[21–35] The use of nanomaterials is especially promising, given their rich physicochemical properties for binding with Aβ aggregates of changing hydrophobicity, as well as their robust capacity for translocation across the blood-brain barrier (BBB).[36] However, it should be noted that the effect of nanoparticle inhibitors on membrane integrity, an essential parameter for assessing their potential as future AD nanomedicines, has not been examined so far in connection with Aβ.

In consideration of the central role of cell membrane in Aβ amyloid aggregation and the crucial need for developing AD nanomedicine, here we examined the membrane fluidity of neuroblastoma SH-SY5Y cells perturbed by Aβ in the three major forms of monomers (Aβ-m), oligomers (Aβ-o) and amyloid fibrils (Aβ-f) as well as their mitigation by ultrasmall molybdenum disulfide (MoS_2) quantum dots (QDs). The ultrasmall MoS_2 QDs were synthesized by bottom-up disordering engineering, a new technique recently developed for obtaining uniform-sized transition metal dichalcogenide QDs.[37] Known for their applications in lubrication, catalysis and bacterial capture,[38] MoS_2 are non-toxic[39] and have been shown as a potent free radical scavenger and a cytokine suppressor.[40–42] Within the field of amyloid mitigation, MoS_2 nanosheets and nanoparticles (100 nm in size) have recently been shown as a multifunctional inhibitor against the aggregation of Aβ and human islet amyloid polypeptide 20–29 ($IAPP_{20–29}$).[43, 44] TPP-MoS_2 nanocomposites (50 nm in size) crossed the BBB and provided efficient neuroprotection through M1/M2 microglial polarization in an Alzheimer's disease model.[45] MoS_2 nanosheets-gold nanorod composites

modulated the aggregation of Aβ, remodeled mature Aβ fibrils under near infrared irradiation, and suppressed Aβ-induced neurotoxicity.[46] Computer simulations, furthermore, revealed that MoS_2 could remodel Aβ fibrils by reducing the hydrogen bonds, hydrophilic and hydrophobic contacts within the fibrils.[47] Compared to other nanomaterials such as graphene sheets and graphene QDs,[31, 48] however, the anti-amyloidogenesis applications of ultrasmall MoS_2 QDs remain unavailable in literature.

In the current study, the membrane fluidity of SH-SY5Y cells exposed to Aβ and ultrasmall MoS_2 QDs was characterized by confocal fluorescence microscopy employing a lipophilic Laurdan dye as an *in situ* molecular reporter. The molecular mechanism of ultrasmall MoS_2 QDs binding with Aβ-o, the Aβ species found to alter membrane fluidity most significantly, was examined in detail using discrete molecular dynamics (DMD) simulations. This study has offered the first evidence of membrane fluidity recovery by an amyloid inhibitor, where ultrasmall MoS_2 QDs exploited their near zero-dimension and surface properties to cage around Aβ into structural formations non-confirmative to the "nanoparticle core/protein corona" convention.[49–51] Taken together, this study provided a crucial basis for arresting the amyloid aggregation and membrane-axis of AD pathology with multifunctional nanomedicine.

MATERIALS AND METHODS

Synthesis of ultrasmall MoS_2 quantum dots.

$MoCl_5$ was dissolved into deionized water by adjusting the pH value to 11 to obtain a Mo-precursor solution. The solution was rendered colorless upon sonication. Then the Mo-precursor solution containing 0.5 mmol Mo was mixed with 40 mL of bovine serum albumin (BSA) solution (1 mg/mL), followed by the addition of 0.2 mL of Na_2S solution (0.5 M) under vigorous stirring at room temperature. The pH of the solution was then adjusted to 6~7 with 1 M HCl. Then, a clear yellow suspension of MoS_2 QDs was formed quickly by pH neutralization. Subsequently, centrifuge filtration tubes with a molecular cut-off of 5,000 Da were utilized to purify the above QDs several times at 4 °C. Lastly, homogeneous ultrasmall MoS_2 QDs with good stability under physiological relevant conditions were obtained.

X-ray diffraction (XRD) and X-ray photoelectron spectroscopy (XPS).

Powder XRD measurements of ultrasmall MoS_2 QDs were performed using a Bruker D8 advanced diffractometer with a Cu Ka irradiation in the 2θ range of 200–600°. The elemental composition and binding energy of the sample were characterized by XPS (AXIS HIS, Kratos Analytical).

Atomic force microscopy (AFM).

A droplet of 20 μL of ultrasmall MoS_2 QDs was deposited on freshly cleaved mica and incubated for 2 min, rinsed with Milli-Q water, and then dried with air. An atomic force microscope (Bruker, Germany) was operated in air at a scan rate of 1 Hz. AFM cantilevers were calibrated on the calibration samples prior to measurements. Selected areas were analyzed for the thickness measurement of the ultrasmall MoS_2 QDs.

ThT fluorescence kinetic assay.

Lyophilized human amyloid-beta ($A\beta_{42}$) monomers (42 residues, DAEFRHDSGYEVHHQKLVFFAEDVGSNKGAIIGLMVGGVVIA, M_W=4,514 Da; purity: 95% by HPLC) was purchased from AnaSpec. Fluorescent thioflavin T (ThT) dye was utilized as a probe to monitor $A\beta_{42}$ (50 μM) amyloid fibril formation. Upon binding to the surface grooves of amyloid fibrils, ThT emitted strong fluorescence at 482 nm. The kinetic fluorescence intensity was recorded by a fluorescence microplate reader for 18 h.

Transmission electron microscopy (TEM).

Ultrasmall MoS_2 QDs and the amyloid fibril formation of $A\beta_{42}$ were imaged with TEM. Hexafluoro-2-propanol treated $A\beta_{42}$ (AnaSpec) was dissolved in 10 μL of 0.1% NH_4OH and then Milli-Q water was added to obtain a stock of 100 μM $A\beta_{42}$. TEM images were acquired with a scanning transmission electron microscope (FEI Tecnai F20 operated at 200 kV) equipped with energy dispersive spectroscopy detectors. 10 μL of samples were placed onto glow-discharged, formvar/carbon-coated copper grids (400 mesh, ProSciTech). After 1 min incubation, the grids were dried on Whatman filter paper followed by a single wash with MilliQ H_2O (5 μL), then negatively stained with 5 μL of uranyl acetate (UA, 1%). The grids were further dried on Whatman filter paper prior to insertion into specimen holders.

Dynamic light scattering.

Hydrodynamic size and zeta potential measurements were performed (Zetasizer Nano-ZS, Malvern). Ultrasmall MoS_2 QDs were suspended in MilliQ H_2O and their hydrodynamic size and zeta potential were measured at room temperature with a He-Ne laser (λ= 632.8 nm).

Fourier-transform infrared (FTIR) spectroscopy.

The secondary structure of $A\beta_{42}$ with or without ultrasmall MoS_2 QDs was determined by FTIR spectroscopy. The peptide samples were incubated in incubator at 37 °C. According to the ThT kinetic assay, $A\beta_{42}$ samples were collected at different time points to cover the three phases of amyloid aggregation: nucleation, elongation, and saturation. The samples (5 μL) were placed onto sample holders and further air-dried. Then the measurements were taken at 20 °C in the wavenumber range of 1570~1730 cm^{-1} through an IRTracer-100 (Shimadzu) equipped with a He-Ne laser and an MCT detector (Hg-Cd-Te) under liquid nitrogen cooling. Peak fitting and data analysis (deconvolution) were performed with Origin Software (Origin Lab) using the built-in PeakDeconvolution application.

Reactive oxygen species (ROS) and cellular viability.

Human neuroblastoma cells (SH-SY5Y) were cultured in Dulbecco's modified Eagle's medium: Nutrient Mixture F-12 (DMEM/F12, ATCC) with the supplement of 10% fetal bovine serum (FBS) at 37 °C and in a 5% CO_2 environment. ~40,000 cells/well were seeded into a 96-well black plate and cultured overnight to reach 80% confluency. ROS detection was performed using an OxiSelect™ intracellular ROS detection kit. SH-SY5Y cells were stained with H_2DCFDA (20 μg/mL) for 30 min and subsequently treated with fresh $A\beta_{42}$ samples in the presence and absence of ultrasmall MoS_2 QDs for 3 h. ROS levels were then

measured indirectly by the oxidation of nonfluorescent DCFDA to fluorescent DCF on a fluorescence microplate reader ClarioStar, excited at 488 nm and detected at 535 nm. All samples were measured in triplicate. Untreated cells were used as negative control and H_2O_2 (200 μM) as positive control.

Cell viability was determined by labelling the SH-SY5Y cells with propidium iodide (1 μM) in DMEM for 30 min before treatment. Cells were treated with different concentrations of ultrasmall MoS_2 QDs and 20 μM of preformed Aβ-o. The percentage of cell death (PI-positive cells) was quantified by an Operetta CLS High-Content Analyzer (PerkinElmer) at 37 °C and 5% CO_2. Nine areas per well were acquired every hour for 24 h. All samples were assayed in triplicate, and untreated cells were used as control. After 48 h treatment, cells were stained by trypan blue at room temperature for 10 min and imaged by an optical microscope.

Quantitative imaging of membrane lipid order.

1.4×10^5 SH-SY5Y cells/well were seeded onto an 8-well chamber slide (μ-Slide, Ibidi) and cultured overnight in a humidified, 37 °C, 5% CO_2 incubator. Lipophilic Laurdan dye (6-Dodecanoyl-2-dimethylaminonaphthalene; MW: 354) with a final concentration of 50 μM was added to each well and allowed to equilibrate with the cell membranes for 1 h. The chamber slide was observed under a Leica SP8 inverted confocal microscope for live fluorescence imaging. The Laurdan dye was excited with laser at 405 nm and its emission read at 430~470 nm (representing gel/liquid ordered phase) or 480~550 nm (representing liquid disordered phase). Cell imaging was performed with a 63×/1.40 numerical aperture oil immersion objective before and after a 3 h-treatment of Aβ species or ultrasmall MoS_2 QDs. Calibration images were acquired through the dye solution without cells, which were recorded with three different laser powers (the same power as used for imaging the sample, as well as a 50% higher power and a 50% lower power).

The acquired images were analyzed by ImageJ software.[52] Generalized polarization (GP) values of cell membranes, expressed analytically as $GP = \frac{I_{400-460} - I_{470-530}}{I_{400-460} + I_{470-530}}$, were then calculated for each pixel of a cell membrane according to our previous protocol.[53] Here $I_{400–460}$ represents the blue light intensity of pixels in the areas of interest from ordered channel images and $I_{470–530}$ represents the green light intensity of pixels from disordered channel images, accordingly. GP shifts were derived by subtraction of the GP distribution peak maximum of each sample with 3 h of incubation from the GP values derived from images taken at the beginning of the experiment (0 h).

Detection of actin filament organization and Aβ-o distribution.

1.4×10^5 SH-SY5Y cells/well were seeded onto 8-well chamber slide (μ-Slide, Ibidi) and cultured overnight in a humidified, 37 °C, 5% CO_2 incubator. Aβ oligomers (20 μM) or ultrasmall MoS_2 QDs (10 and 100 μM) were incubated with cells for 3 h. Cell culture media were used as negative control. Cells were gently washed twice with phosphate-buffered saline (PBS), and 4% of paraformaldehyde was added to fix the cells at room temperature for 15 min. After that, immunofluorescent staining was performed to reveal the distribution

and organization of Aβ-o and actin filaments. Primary rabbit anti-oligomer polyclonal antibody (Invitrogen, 1:400) was incubated with the cells at 4 °C overnight, then donkey anti-rabbit Alex 594 secondary antibody (Abcam, 1:500) was used to conjugate with the primary antibody at room temperature for 2 h. Actin filaments were labelled with phalloidin-iFluor 488 (Abcam, 1:1000) at the same time. Then the cells were washed with PBS and further stained by Hoechst 33342 (Sigma, 2 μg/mL) for 5 min. After washing twice with PBS, the cells were observed with a Leica SP8 inverted confocal fluorescence microscope.

Statistical analysis.

Data are represented as means (n=3) ± standard errors of the mean (SEM). Statistical analysis was performed through unpaired *t*-test determining two tailed *P*-values. A P value < 0.05 was considered statistically significant.

Molecular dynamics simulations.

Computer simulations were performed with the all-atom discrete molecular dynamics (DMD). The continuous interaction potentials in classic molecular dynamics were replaced by discrete stepwise functions in DMD.[54] Collisions occurred when two atoms met at an energy step and their velocities were updated according to conservation laws. Thus, the system's dynamics in DMD was dictated by iteratively updating only the two colliding atoms, predicting their new collisions with corresponding neighbors, and finding the next collision via quick sort algorithms. Compared with classic molecular dynamics, the sampling efficiency of DMD is significantly enhanced and has been used by us and others to study protein folding, amyloid aggregation, and interactions with nanoparticles.[30, 55, 56] Interatomic interactions including bonded interactions (i.e., covalent bonds, bond angles, and dihedrals) and non-bonded interactions (i.e., van der Waals, solvation, hydrogen bond, and electrostatic terms) in our all-atom DMD simulations were adapted from the Medusa force field, which was benchmarked for accurate prediction of protein stability change upon mutation and protein–ligand binding affinity.[57, 58] The force field parameters for van der Waals, covalent bonds, bond angles, and dihedrals were taken from CHARMM force field.[59] Solvation was implicitly modelled by the effective energy function proposed by Lazaridis and Karplus.[60] The distance- and angle-dependent hydrogen bond interactions were modelled by a reaction-like algorithm.[61] The screened electrostatic interactions were computed using the Debye–Huckel approximation with the Debye length set to 10 Å, corresponding to a monovalent salt concentration of 100 mM.

The initial structures of Aβ-m and Aβ-f were taken from protein databank (PDB ID: 1Z0Q and 5OQV, respectively). A square ultrasmall MoS_2 QD with an edge length of 2.6 nm (*cf.* Figure 5A), consisting of 255 atoms, was constructed. The recently developed force field of MoS_2 based on the experimental monolayered water contact angle was incorporated in Medusa.[62, 63] The initial structure of the ultrasmall MoS_2 QD was relaxed with a 100 ns simulation. For each system, 30 independent simulations with different initial configurations and velocities were performed, each of which lasted 400 ns at 300 K. A cubic box with periodic boundary condition was used and the dimension of the box was set to maintain the concentration of Aβ peptides the same as that of a single peptide in a cubic box with the dimension of 7.5 nm.

Computational analysis.

The peptide secondary structure was calculated using the dictionary secondary structure of protein (DSSP) program.[64] A hydrogen bond was considered to be formed if the distance between the backbone N and O atoms within 3.5 Å and the angle of NH···O was larger than 120°. Residue-residue and residue-MoS_2 contact were defined if they had at least one heavy atom contact within the cutoff distance of 0.55 nm. The two-dimensional potential of mean force (PMF) was computed as $-k_BT\ln P(R_g, N_{\mathrm{Hbond}})$, where $P(R_g, N_{\mathrm{Hbond}})$ denoted the probability of a conformation having a given value of radius of gyration, R_g, and the total number of inter-peptide hydrogen bonds (N_{Hbond}).

2. RESULTS AND DISCUSSION

Characterizations of ultrasmall MoS_2 quantum dots

Ultrasmall MoS_2 QDs were prepared by a modified Ding-Leong method[37] in aqueous condition at room temperature though a simple chemical reaction, as illustrated in Figure 1. Transmission electron microscopy (TEM) and atomic force microscopy (AFM) were used to characterize the structure and morphology of the ultrasmall MoS_2 QDs. As presented in Figure 1A, typical TEM image of ultrasmall MoS_2 QDs exhibited good dispersibility and a uniform size distribution with an average size of 2.2 ± 0.7 nm. The thickness of the ultrasmall MoS_2 QDs was measured by AFM to be 0.5~3.5 nm, with majority below 2 nm (Figure S1). Dynamic light scattering (DLS) indicated the hydrodynamic diameter of the ultrasmall MoS_2 QDs at ~4 nm, with a polydispersity of 0.21 and a zeta potential value of −7.0±2.8 mV (Figure 1B&C). The crystal structure of as-synthesized ultrasmall MoS_2 QDs was further characterized by powder X-ray diffraction (XRD) spectroscopy. As shown in Figure 1D, the corresponding XRD pattern exhibited broad diffraction peaks, similar to the XRD character of the low-dimensional MoS_2 indicating the small size of the QDs. The two weak peaks at 2θ≈30.3° and 40.2° were assigned to the featured (100) and (103) faces of hexagonal MoS_2 (JCPDS NO. 24–0513), respectively. The chemical states of ultrasmall MoS_2 QDs were explored by X-ray photoelectron spectroscopy (XPS) measurements. The Mo 3d, S 2s, and S 2p regions of the XPS spectrum for samples are shown in Figure 1E&F. In the Mo 3d spectrum, the two peaks at 230.9 eV and 233.9 eV corresponded to the Mo 3d5/2 and 3d3/2 respectively, and the peak at 227.9 eV was assigned to S 2s, suggesting that the dominance of Mo^{4+} oxidation state. Correspondingly, sulfur displayed two different chemical states as shown in Figure 1F. The two peaks at 161.7 and 164.7 eV were allocated to the S 2p3/2 and S 2p1/2 orbitals of divalent sulfide ions. Furthermore, an additional peak at a higher binding energy of 167.4 eV was assigned to the sulfate composite, in which S-O bond existed, indicating partial oxidation of the S edges generated in the experiment process. The toxicity of ultrasmall MoS_2 QDs was further validated *in vitro* by ROS detection and cellular viability assay, where SH-SY5Y cells were exposed to different concentrations of MoS_2 QDs (Figure 1G&H). The ROS production induced by ultrasmall MoS_2 QDs was comparable to non-treated cells in 3 h-exposure, and almost no cell death after 24 h and 48 h exposure (Figure S2).

Inhibition of Aβ fibrillization by ultrasmall MoS_2 quantum dots

The structural and composition characteristics of Aβ-o as heterogeneous α-helical to β-sheet transitional aggregates have been examined extensively in the literature.[65–77] Here, the self-assembly of Aβ featured a sigmoidal curve to evolve from monomeric (Aβ-m) to oligomeric (Aβ-o) and fibrillar species (Aβ-f). ThT fluorescence kinetic assay and TEM imaging were used to monitor the aggregation process and the morphology of Aβ species in the presence and absence of ultrasmall MoS_2 QDs. As shown in Figure 2A, freshly dissolved monomeric Aβ could assemble into oligomers at ~12 h (Figure S3) and further developed into fibrils within 15 h. When Aβ was incubated with ultrasmall MoS_2 QDs at 1:0.5 and 1:5 molar ratios, this well-characterized aggregation process of Aβ became significantly inhibited (Figures 2A&S4). This inhibiting capacity of ultrasmall MoS_2 QDs is essential for their further development into an AD nanomedicine.

FTIR spectroscopy further demonstrated the inhibition capacity of ultrasmall MoS_2 QDs based on the secondary structure of Aβ in aggregation (Figures 2B, S5&S6, Table S1). The contents of α-helix/disordered, β-sheet and β-turn of the Aβ species were derived through the amide-bond deconvolution of their FTIR peaks.[78] Specifically, Aβ exhibited a conversion of α-helical structures (39.6 %) at 1 h to β-sheets (61.6%) after 30 h incubation in H_2O and at 37 °C due to fibrillization. The inhibition of β-sheet formation was found with the presence of ultrasmall MoS_2 QDs at the 1:5 molar ratio after 30 h, yielding secondary structures of β-sheets (43.6%), α-helices/disordered (42.6%) and β-turns (13.8%). In addition, the secondary structure contents were comparable to that of monomeric Aβ (1 h), including β-sheets (47.1%), α-helix/disordered (39.6%) and β-turns (13.3%). Therefore, ultrasmall MoS_2 QDs could sustain Aβ in its monomeric state. TEM imaging further validated the results of the Aβ samples with MoS_2, which was recorded at 12, 30 h incubation (Figure 2C–G). In comparison to Aβ itself, the Aβ samples with ultrasmall MoS_2 QDs rendered small numbers of shorter and softer fibrils, mostly devoid of rigid mature fibrils. As shown in Figure 2F&G, the most abundant Aβ species were monomeric-like at the molar ratio of 1:5.

Disruption of membrane fluidity by Aβ and its rescue by ultrasmall MoS_2 quantum dots

Among all the Aβ species, Aβ-o was found to be the most toxic and displayed a greater membrane affinity than the monomers or fibrils,[79] which could induce membrane reorganization, deformation, pore formation via increased permeabilization and lipid extraction.[10] Generalized polarization (GP) values were adopted in this study to evaluate changes to membrane fluidity between the membrane ordered and disordered phases *in vitro* (Figure 3A).[52, 53]

When the SH-SY5Y cells were exposed to Aβ species around 3 h, a large positive GP shift was observed with Aβ-o (+0.1526), demonstrating an increased membrane lipid order and disruption of membrane fluidity (Figure 3B&C). Aβ-o could partition into the membranes after their association with the cells, which was accompanied by a general increase of lateral spreading of lipid headgroups and more ordered membrane performance.[15, 80, 81] Alternatively, Aβ could be a perforating agent and further induce channel-like perforation in neuronal cell membranes, causing an increase of the membrane order.[13, 82] These accounted

for the largest positive GP shift mediated by Aβ-o.[10] Interestingly, the cell membrane order (+0.0283) revealed a significant decrease by the combination of Aβ-o and ultrasmall MoS_2 QDs at the molar ratio of 1:0.5 (Figure 3D). Then the membrane order (−0.0032) was further restored to the control cell level with the increasing amount of MoS_2 QDs at the molar ratio of 1:5 (Figure 3E). Furthermore, MoS_2 QDs were added to cells pre-incubated for 1 h with Aβ-o, and the nanostructures were still able to recover the perturbed membrane fluidity after 3 h of incubation (Figures S7). The cell membrane fluidity did not change by the treatment of Aβ-m (+0.0344), Aβ-f (+0.0091), or for cells incubated with ultrasmall MoS_2 QDs only (10 μM, +0.0070; 100 μM, −0.0143) (Figures 3B&S8). Therefore, ultrasmall MoS_2 QDs could obviously rescue membrane disruption induced by Aβ-o. One reason for such phenomenon was that ultrasmall MoS_2 QDs possessed a high affinity for Aβ-o via hydrophilic interactions and a high surface area, which hindered further Aβ-o-membrane interaction or Aβ-Aβ aggregation. To investigate the association of Aβ-o and ultrasmall MoS_2 QDs under the circumstance with cells, Aβ-o distribution was observed after 3 h exposure to SH-SY5Y cells in the presence and absence of ultrasmall MoS_2 QDs (Figures S9&S10). Aβ-o were mainly located around the cell membranes and cytoplasm after 3 h. With increased presence of ultrasmall MoS_2 QDs, less Aβ-o were then spotted around cell membranes (Figure S9A). At the ratio of 1:5, the intensity of Aβ-o recorded a notable decrease compared to the group without ultrasmall MoS_2 QDs (Figure S9B). This verified that additional ultrasmall MoS_2 QDs could prevent the association of Aβ with cell membrane and further rescue Aβ disruption to the latter.

In addition, cell exposure to Aβ-o also led to the increased intensity of actin filaments at 1 and 3 h incubation, while the addition of ultrasmall MoS_2 QDs mitigated elevation of actin expression at 3 h (Figures 4A, B&S11). Although 20 μM of Aβ-o did not generate a considerable amount of ROS at 3 h, they still caused 20% cell death after 20 h treatment (Figure 4C&D). With the combination of Aβ-o and ultrasmall MoS_2 QDs, cell toxicity was significantly alleviated after 20 h with both ratios of 1:0.5 and 1:5 compared to Aβ-o ($P<0.001$). The Aβ sequestration by ultrasmall MoS_2 QDs could be the main reason for the alleviated actin reorganization and cell death. The interaction mechanism of Aβ and ultrasmall MoS_2 QDs was further investigated by DMD simulations.

Dynamics of Aβ-MoS_2 interaction by discrete molecular dynamics simulations

All-atom simulations were performed to investigate the inhibition mechanism of ultrasmall MoS_2 QDs on Aβ aggregation. In accordance with the *in vitro* experiments, the interactions of ultrasmall MoS_2 QDs with Aβ-m, preformed Aβ-o and Aβ-f were systematically simulated. The concentration ratios between Aβ and MoS_2 QDs were set to be 4:4 and 4:8 to reduce the computational cost associated with modeling a large quantity of MoS_2 QDs. For the self-assembly of four Aβ-m in the absence of ultrasmall MoS_2 QDs, stable tetramers were formed in most of the independent simulations (Figure 5B). When incubated with equimolar ultrasmall MoS_2 QDs, Aβ peptides remained in the monomeric state, or aggregated into dimers, trimers and tetramers with similar propensities. In contrast, Aβ tetramers could no longer be formed when co-aggregated with eight ultrasmall MoS_2 QDs. In addition, the overall β-sheet content was reduced while the coil and bend structure contents increased in the presence of ultrasmall MoS_2 QDs (Figure 5C). Taken together, our

simulations indicated that ultrasmall MoS_2 QDs can effectively reduce the Aβ-o size and inhibit the Aβ aggregation process, consistent with the experimental observations (Figure 2).

To elucidate the underlying mechanism of the inhibition effects of ultrasmall MoS_2 QDs on Aβ aggregation, the binding frequency of ultrasmall MoS_2 QDs with each Aβ residue and the contact frequency maps between Aβ peptides were calculated. Driven by hydrophilic interactions, ultrasmall MoS_2 QDs displayed a strong binding affinity with the hydrophilic N-terminus of Aβ, whereas the binding affinity with the hydrophobic C-terminus was relatively weak (Figure 5D). This is consistent with the experimental observation that affinity between ultrasmall MoS_2 QDs and hydrophilic $IAPP_{20–29}$ was stronger than that with hydrophobic $Aβ_{33–42}$.[43] Upon binding with ultrasmall MoS_2 QDs, the inter-peptide contact frequency was significantly reduced compared with control (Figure 5E&F). Thus, ultrasmall MoS_2 QDs inhibited the aggregation of Aβ peptides by binding with the N-terminus of Aβ peptide, sequestering the small-size oligomers and effectively reducing the inter-peptide contact.

To further probe the conformational properties of Aβ peptides in the presence of ultrasmall MoS_2 QDs, the two-dimensional potential of mean force (PMF) with respect to the number of inter-peptide hydrogen bonds (H-bond) and averaged radius of gyration (R_g) of Aβ peptides were calculated (Figure 5G&H). In the absence of the ultrasmall MoS_2 QDs, the PMF featured a great number of inter-peptide hydrogen bonds. In the presence of ultrasmall MoS_2 QDs, however, the free energy basins became narrower and the number of inter-peptide hydrogen bonds decreased to 0, 11 and 13 respectively for the three basins. Meanwhile, Aβ peptides were more compact in the presence of ultrasmall MoS_2 QDs as indicated by the smaller value of R_g. This was confirmed by the typical conformations near the free energy surface basins that the Aβ peptides were confined by the cells formed by ultrasmall MoS_2 QDs.

To further investigate the effects of the nanostructure on Aβ-o, ultrasmall MoS_2 QDs were added to preformed Aβ tetramers with molar ratios of peptide/MoS_2 set at 4:4 and 4:8. Interestingly, the β-sheet content, Aβ oligomer size and inter-peptide hydrogen bonds kept almost unchanged in the presence of ultrasmall MoS_2 QDs compared with the control, suggesting that ultrasmall MoS_2 QDs could not dissociate the preformed Aβ-o. Instead, the ultrasmall MoS_2 QDs bound on the surfaces of Aβ tetramers, as indicated by the radial distribution function of atoms of Aβ peptides and ultrasmall MoS_2 QDs (Figure 6A&B). For the systems with four ultrasmall MoS_2 QDs, all four QDs bound on the surfaces of Aβ tetramers in most of the independent simulations (Figure 6C). When eight ultrasmall MoS_2 QDs were added to the Aβ tetramers, the number of QDs bound on the tetramers ranged from four to eight (Figure 6D), which suggested that the surfaces of Aβ tetramers were sufficiently large to bind at least four ultrasmall MoS_2 QDs. The slightly negative zeta potential of the MoS_2 QDs observed in the experiments resulted from the partial charges of un-saturated sulphur atoms at the edges of the nanosheets. The weak electrostatic interactions between the ultrasmall MoS_2 QDs and Aβ-m and Aβ-o could re-orientate the Aβ peptides on the nanostructure surfaces but without affecting their binding,[47] and thus, the formation of testudo-like, reverse protein-corona structures as predicted by the simulations. Therefore, the ultrasmall MoS_2 QDs inhibited the aggregation process of Aβ-o by forming a

protective testudo-like shell outside the oligomers to hinder the further aggregation process (Figure 6E&F), which was distinct from the inhibition mechanism on Aβ-m. Such unusual mechanism with the "protein core-nanoparticle corona" formed with ultrasmall MoS_2 QDs was also quite different from the sequestration/adsorption effects of large-size MoS_2 nanosheets.[43–47, 83, 84] Hence, it may be inferred from the simulations that the disruption of cell membranes could be ameliorated by the association of Aβ-o with ultrasmall MoS_2 QDs.[85]

To understand the conformation of Aβ-f interacting with ultrasmall MoS_2 QDs, the binding between a 20-peptide Aβ-f with equimolar ultrasmall MoS_2 QDs was simulated. To reduce the computational cost for such a large molecular system, we constrained the movement of Aβ-f and allowed the ultrasmall MoS_2 QDs to move freely. The conformations of the Aβ-f-MoS_2 showed that the QDs could bind both the ends and side-walls of the fibrils (Figure S12), indicating that elongation and secondary nucleation processes would be hindered by the ultrasmall MoS_2 QDs. Therefore, similarly to the case with Aβ-o, the direct interaction between Aβ-f and cell membranes could also be attenuated by the fibrillar coating of ultrasmall MoS_2 QDs.

Conclusion

Understanding the interaction between amyloid peptide and cell membrane plays a central role in delineating the pathogenesis of AD as well as a range of amyloid diseases. As increasing efforts have been dedicated to the development of AD nanomedicine, it has become crucial to examine the membrane-axis of AD taking into consideration of the additional roles exerted by the nanoparticle inhibitors.[4, 10, 48] In this study, we set to study for the mitigation potential of a newly developed nanomaterial, namely ultrasmall MoS_2 QDs, against Aβ amyloid aggregation. We further studied the membrane fluidity of neuronal cells perturbed by Aβ in its monomeric, oligomeric and fibrillar forms. We found the oligomeric peptide Aβ-o at 20 μM and after 3 h of cell incubation exerted the most significant shift of GP = 0.1526 with an *in situ* Laurdan dye reporter, while the aberrant change in membrane fluidity was completely recovered to GP = −0.0032 with the introduction of ultrasmall MoS_2 QDs at a molar ratio of Aβ-o/MoS_2 of 1:5. With confocal fluorescence imaging we observed a reduction in cell association of Aβ-o in conjunction with the increased presence of ultrasmall MoS_2 QDs, suggesting Aβ-o bound with the nanostructure of comparable size to halt their perturbation to cell membrane (Figure 7). This phenomenon was coupled with a reduction in actin expression that was elevated by cell exposure to the toxic oligomeric peptide, indicating an intracellular consequence of peptide exposure and their effective recovery with the nanomaterial (Figure 7). Our DMD simulations further revealed the differential binding mechanisms of the three major Aβ species with ultrasmall MoS_2 QDs. Specifically, hydrophilic interactions occurred between the MoS_2 QDs and the N-terminus of Aβ-m. In contrast, surface adsorption of Aβ-o and Aβ-f onto MoS_2 QDs rendered testudo-like, reverse protein-corona formations to discourage the peptide-cell membrane association. Such unusual "protein core-nanoparticle corona" formations have not been reported before for amyloid inhibition with nanomaterials and were rendered feasible in this study by the comparable size of Aβ-o and the ultrasmall MoS_2 QDs, as well as by the specific physicochemical properties of the peptide species and the

nanostructure. This interfacial study offered a crucial new insight and a facile strategy for manipulating the membrane-axis of AD pathology with tailor-designed AD nanomedicines.

Supplementary Material

Refer to Web version on PubMed Central for supplementary material.

Acknowledgements

This work was supported by ARC Project CE140100036 (Davis), NSF CAREER CBET-1553945 (Ding) and NIH MIRA R35GM119691 (Ding).

References:

(1). Long JM; Holtzman DM, Alzheimer Disease: An Update on Pathobiology and Treatment Strategies. Cell 2019, 179, 312–339. [PubMed: 31564456]

(2). Hardy JA; Higgins GA, Alzheimer's Disease: The Amyloid Cascade Hypothesis. Science 1992, 256, 184–185. [PubMed: 1566067]

(3). Ferreira ST; Klein WL, The Aβ Oligomer Hypothesis for Synapse Failure and Memory Loss in Alzheimer's Disease. Neurobiol. Learn. Mem 2011, 96, 529–543.

(4). Ke PC; Zhou R; Serpell LC; Riek R; Knowles TPJ; Lashuel HA; Gazit E; Hamley IW; Davis TP; Fändrich M; Otzen DE; Chapman MR; Dobson CM; Eisenberg DS; Mezzenga R, Half a Century of Amyloids: Past, Present and Future. Chem. Soc. Rev 2020, 49, 5473–5509. [PubMed: 32632432]

(5). Leyns CE0047; Ulrich JD; Finn MB; Stewart FR; Koscal LJ; Remolina Serrano J; Robinson GO; Anderson E; Colonna M; Holtzman DM, Trem2 Deficiency Attenuates Neuroinflammation and Protects against Neurodegeneration in a Mouse Model of Tauopathy. Proc. Natl. Acad. Sci. U.S.A 2017, 114, 11524–11529. [PubMed: 29073081]

(6). de Calignon A; Polydoro M; Suárez-Calvet M; William C; Adamowicz DH; Kopeikina KJ; Pitstick R; Sahara N; Ashe KH; Carlson GA; Spires-Jones TL; Hyman BT, Propagation of Tau Pathology in a Model of Early Alzheimer's Disease. Neuron 2012, 73, 685–697. [PubMed: 22365544]

(7). Butterfield SM; Lashuel HA, Amyloidogenic Protein-Membrane Interactions: Mechanistic Insight from Model Systems. Angew. Chem. Int. Ed. Engl 2010, 49, 5628–5654. [PubMed: 20623810]

(8). Eckert GP; Wood WG; Muller WE, Lipid Membranes and β-Amyloid: A Harmful Connection. Curr. Protein Pept. Sci 2010, 11, 319–325. [PubMed: 20423299]

(9). Ambroggio EE; Kim DH; Separovic F; Barrow CJ; Barnham KJ; Bagatolli LA; Fidelio GD, Surface Behavior and Lipid Interaction of Alzheimer β-Amyloid Peptide 1–42: A Membrane-Disrupting Peptide. Biophys. J 2005, 88, 2706–2713. [PubMed: 15681641]

(10). Li Y; Tang H; Andrikopoulos N; Javed I; Cecchetto L; Nandakumar A; Kakinen A; Davis TP; Ding F; Ke PC, The Membrane Axis of Alzheimer's Nanomedicine. Adv. NanoBiomed Res 2021, 1, 2000040. [PubMed: 33748816]

(11). Nagarathinam A; Hoflinger P; Buhler A; Schafer C; McGovern G; Jeffrey M; Staufenbiel M; Jucker M; Baumann F, Membrane-Anchored Abeta Accelerates Amyloid Formation and Exacerbates Amyloid-Associated Toxicity in Mice. J. Neurosci 2013, 33, 19284–19294. [PubMed: 24305824]

(12). Ke PC; Sani MA; Ding F; Kakinen A; Javed I; Separovic F; Davis TP; Mezzenga R, Implications of Peptide Assemblies in Amyloid Diseases. Chem. Soc. Rev 2017, 46, 6492–6531. [PubMed: 28702523]

(13). Sepulveda FJ; Parodi J; Peoples RW; Opazo C; Aguayo LG, Synaptotoxicity of Alzheimer Beta Amyloid Can Be Explained by Its Membrane Perforating Property. PLoS One 2010, 5, e11820. [PubMed: 20676404]

(14). Fabiani C; Antollini SS, Alzheimer's Disease as a Membrane Disorder: Spatial Cross-Talk among Beta-Amyloid Peptides, Nicotinic Acetylcholine Receptors and Lipid Rafts. Front. Cell. Neurosci 2019, 13, 309. [PubMed: 31379503]

(15). Williams TL; Serpell LC, Membrane and Surface Interactions of Alzheimer's Abeta Peptide--Insights into the Mechanism of Cytotoxicity. FEBS J. 2011, 278, 3905–3917. [PubMed: 21722314]

(16). Bode DC; Freeley M; Nield J; Palma M; Viles JH, Amyloid-Beta Oligomers Have a Profound Detergent-Like Effect on Lipid Membrane Bilayers, Imaged by Atomic Force and Electron Microscopy. J Biol Chem 2019, 294, 7566–7572. [PubMed: 30948512]

(17). Serra-Batiste M; Ninot-Pedrosa M; Bayoumi M; Gairi M; Maglia G; Carulla N, Abeta42 Assembles into Specific Beta-Barrel Pore-Forming Oligomers in Membrane-Mimicking Environments. Proc. Natl. Acad. Sci. U.S.A 2016, 113, 10866–10871. [PubMed: 27621459]

(18). Poojari C; Kukol A; Strodel B, How the Amyloid-Beta Peptide and Membranes Affect Each Other: An Extensive Simulation Study. Biochim. Biophys. Acta 2013, 1828, 327–339. [PubMed: 22975281]

(19). Ciudad S; Puig E; Botzanowski T; Meigooni M; Arango AS; Do J; Mayzel M; Bayoumi M; Chaignepain S; Maglia G; Cianferani S; Orekhov V; Tajkhorshid E; Bardiaux B; Carulla N, Abeta(1–42) Tetramer and Octamer Structures Reveal Edge Conductivity Pores as a Mechanism for Membrane Damage. Nat. Commun 2020, 11, 3014. [PubMed: 32541820]

(20). Flagmeier P; De S; Wirthensohn DC; Lee SF; Vincke C; Muyldermans S; Knowles TPJ; Gandhi S; Dobson CM; Klenerman D, Ultrasensitive Measurement of Ca(2+) Influx into Lipid Vesicles Induced by Protein Aggregates. Angew. Chem. Int. Ed. Engl 2017, 56, 7750–7754. [PubMed: 28474754]

(21). Lansbury PT; Lashuel HA, A Century-Old Debate on Protein Aggregation and Neurodegeneration Enters the Clinic. Nature 2006, 443, 774–779. [PubMed: 17051203]

(22). McLaurin J; Cecal R; Kierstead ME; Tian X; Phinney AL; Manea M; French JE; Lambermon MHL; Darabie AA; Brown ME; Janus C; Chishti MA; Horne P; Westaway D; Fraser PE; Mount HTJ; Przybylski M; St George-Hyslop P, Therapeutically Effective Antibodies against Amyloid-β Peptide Target Amyloid-β Residues 4–10 and Inhibit Cytotoxicity and Fibrillogenesis. Nat. Med 2002, 8, 1263–1269. [PubMed: 12379850]

(23). Bieschke J; Herbst M; Wiglenda T; Friedrich RP; Boeddrich A; Schiele F; Kleckers D; Lopez del Amo JM; Grüning BA; Wang Q; Schmidt MR; Lurz R; Anwyl R; Schnoegl S; Fändrich M; Frank RF; Reif B; Günther S; Walsh DM; Wanker EE, Small-Molecule Conversion of Toxic Oligomers to Nontoxic β-Sheet–Rich Amyloid Fibrils. Nat. Chem. Biol 2011, 8, 93–101. [PubMed: 22101602]

(24). Cabaleiro-Lago C; Quinlan-Pluck F; Lynch I; Lindman S; Minogue AM; Thulin E; Walsh DM; Dawson KA; Linse S, Inhibition of Amyloid Beta Protein Fibrillation by Polymeric Nanoparticles. J. Am. Chem. Soc 2008, 130, 15437–15443. [PubMed: 18954050]

(25). Gurzov EN; Wang B; Pilkington EH; Chen P; Kakinen A; Stanley WJ; Litwak SA; Hanssen EG; Davis TP; Ding F; Ke PC, Inhibition of Hiapp Amyloid Aggregation and Pancreatic Beta-Cell Toxicity by Oh-Terminated Pamam Dendrimer. Small 2016, 12, 1615–1626. [PubMed: 26808649]

(26). Gao N; Sun H; Dong K; Ren J; Duan T; Xu C; Qu X, Transition-Metal-Substituted Polyoxometalate Derivatives as Functional Anti-Amyloid Agents for Alzheimer's Disease. Nat. Commun 2014, 5, 3422. [PubMed: 24595206]

(27). Luo Q; Lin YX; Yang PP; Wang Y; Qi GB; Qiao ZY; Li BN; Zhang K; Zhang JP; Wang L; Wang H, A Self-Destructive Nanosweeper That Captures and Clears Amyloid Beta-Peptides. Nat. Commun 2018, 9, 1802. [PubMed: 29728565]

(28). Zhao Y; Cai J; Liu Z; Li Y; Zheng C; Zheng Y; Chen Q; Chen H; Ma F; An Y; Xiao L; Jiang C; Shi L; Kang C; Liu Y, Nanocomposites Inhibit the Formation, Mitigate the Neurotoxicity, and Facilitate the Removal of β-Amyloid Aggregates in Alzheimer's Disease Mice. Nano Lett. 2019, 19, 674–683. [PubMed: 30444372]

(29). Chen Q; Du Y; Zhang K; Liang Z; Li J; Yu H; Ren R; Feng J; Jin Z; Li F; Sun J; Zhou M; He Q; Sun X; Zhang H; Tian M; Ling D, Tau-Targeted Multifunctional Nanocomposite for

Combinational Therapy of Alzheimer's Disease. ACS Nano 2018, 12, 1321–1338. [PubMed: 29364648]

(30). Javed I; Peng G; Xing Y; Yu T; Zhao M; Kakinen A; Faridi A; Parish CL; Ding F; Davis TP; Ke PC; Lin S, Inhibition of Amyloid Beta Toxicity in Zebrafish with a Chaperone-Gold Nanoparticle Dual Strategy. Nat. Commun 2019, 10, 3780. [PubMed: 31439844]

(31). Mahmoudi M; Akhavan O; Ghavami M; Rezaee F; Ghiasi SM, Graphene Oxide Strongly Inhibits Amyloid Beta Fibrillation. Nanoscale 2012, 4, 7322–7325. [PubMed: 23079862]

(32). Gladytz A; Abel B; Risselada HJ, Gold-Induced Fibril Growth: The Mechanism of Surface-Facilitated Amyloid Aggregation. Angew. Chem. Int. Ed 2016, 55, 11242–11246.

(33). Javed I; Yu T; Peng G; Sanchez-Ferrer A; Faridi A; Kakinen A; Zhao M; Mezzenga R; Davis TP; Lin S; Ke PC, In Vivo Mitigation of Amyloidogenesis through Functional-Pathogenic Double-Protein Coronae. Nano Lett. 2018, 18, 5797–5804. [PubMed: 30088935]

(34). Brender JR; Salamekh S; Ramamoorthy A, Membrane Disruption and Early Events in the Aggregation of the Diabetes Related Peptide Iapp from a Molecular Perspective. Acc. Chem. Res 2012, 45, 454–462. [PubMed: 21942864]

(35). Kotler SA; Walsh P; Brender JR; Ramamoorthy A, Differences between Amyloid-β Aggregation in Solution and on the Membrane: Insights into Elucidation of the Mechanistic Details of Alzheimer's Disease. Chem. Soc. Rev 2014, 43, 6692–6700. [PubMed: 24464312]

(36). Chen P; Ding F; Cai R; Javed I; Yang W; Zhang Z; Li Y; Davis TP; Ke PC; Chen C, Amyloidosis Inhibition, a New Frontier of the Protein Corona. Nano Today 2020, 35, 100937. [PubMed: 32728376]

(37). Ding X; Peng F; Zhou J; Gong W; Slaven G; Loh KP; Lim CT; Leong DT, Defect Engineered Bioactive Transition Metals Dichalcogenides Quantum Dots. Nat. Commun 2019, 10, 41. [PubMed: 30604777]

(38). Wang L; Gao F; Wang A; Chen X; Li H; Zhang X; Zheng H; Ji R; Li B; Yu X; Liu J; Gu Z; Chen F; Chen C, Defect-Rich Adhesive Molybdenum Disulfide/Rgo Vertical Heterostructures with Enhanced Nanozyme Activity for Smart Bacterial Killing Application. Adv. Mater 2020, 32, 2005423.

(39). Wu H; Yang R; Song B; Han Q; Li J; Zhang Y; Fang Y; Tenne R; Wang C, Biocompatible Inorganic Fullerene-Like Molybdenum Disulfide Nanoparticles Produced by Pulsed Laser Ablation in Water. ACS Nano 2011, 5, 1276–1281. [PubMed: 21230008]

(40). Wang T; Zhu H; Zhuo J; Zhu Z; Papakonstantinou P; Lubarsky G; Lin J; Li M, Biosensor Based on Ultrasmall MoS2 Nanoparticles for Electrochemical Detection of H2o2 Released by Cells at the Nanomolar Level. Anal. Chem 2013, 85, 10289–10295. [PubMed: 24067077]

(41). Zhang XD; Zhang J; Wang J; Yang J; Chen J; Shen X; Deng J; Deng D; Long W; Sun YM; Liu C; Li M, Highly Catalytic Nanodots with Renal Clearance for Radiation Protection. ACS Nano 2016, 10, 4511–4519. [PubMed: 27018632]

(42). Pardo M; Shuster-Meiseles T; Levin-Zaidman S; Rudich A; Rudich Y, Low Cytotoxicity of Inorganic Nanotubes and Fullerene-Like Nanostructures in Human Bronchial Epithelial Cells: Relation to Inflammatory Gene Induction and Antioxidant Response. Environ. Sci. Technol 2014, 48, 3457–3466. [PubMed: 24533583]

(43). Wang J; Liu L; Ge D; Zhang H; Feng Y; Zhang Y; Chen M; Dong M, Differential Modulating Effect of MoS2 on Amyloid Peptide Assemblies. Chem. Eur. J 2018, 24, 3397–3402. [PubMed: 29210123]

(44). Han Q; Cai S; Yang L; Wang X; Qi C; Yang R; Wang C, Molybdenum Disulfide Nanoparticles as Multifunctional Inhibitors against Alzheimer's Disease. ACS Appl. Mater. Interfaces 2017, 9, 21116–21123. [PubMed: 28613069]

(45). Ren C; Li D; Zhou Q; Hu X, Mitochondria-Targeted Tpp-MoS2 with Dual Enzyme Activity Provides Efficient Neuroprotection through M1/M2 Microglial Polarization in an Alzheimer's Disease Model. Biomaterials 2020, 232, 119752. [PubMed: 31923845]

(46). Wang X; Han Q; Liu X; Wang C; Yang R, Multifunctional Inhibitors of β-Amyloid Aggregation Based on MoS2/Aunr Nanocomposites with High near-Infrared Absorption. Nanoscale 2019, 11, 9185–9193. [PubMed: 31038146]

(47). Mudedla SK; Murugan NA; Subramanian V; Agren H, Destabilization of Amyloid Fibrils on Interaction with MoS2-Based Nanomaterials. RSC Adv. 2019, 9, 1613–1624.

(48). Andrikopoulos N; Li Y; Cecchetto L; Nandakumar A; Da Ros T; Davis TP; Velonia K; Ke PC, Nanomaterial Synthesis, an Enabler of Amyloidosis Inhibition against Human Diseases. Nanoscale 2020, 12, 14422–14440. [PubMed: 32638780]

(49). Radic S; Nedumpully-Govindan P; Chen R; Salonen E; Brown JM; Ke PC; Ding F, Effect of Fullerenol Surface Chemistry on Nanoparticle Binding-Induced Protein Misfolding. Nanoscale 2014, 6, 8340–8349. [PubMed: 24934397]

(50). Ratnikova TA; Nedumpully Govindan P; Salonen E; Ke PC, In Vitro Polymerization of Microtubules with a Fullerene Derivative. ACS Nano 2011, 5, 6306–6314. [PubMed: 21761844]

(51). Cedervall T; Lynch I; Lindman S; Berggård T; Thulin E; Nilsson H; Dawson KA; Linse S, Understanding the Nanoparticle–Protein Corona Using Methods to Quantify Exchange Rates and Affinities of Proteins for Nanoparticles. Proc. Natl. Acad. Sci. U.S.A 2007, 104, 2050–2055. [PubMed: 17267609]

(52). Owen DM; Rentero C; Magenau A; Abu-Siniyeh A; Gaus K, Quantitative Imaging of Membrane Lipid Order in Cells and Organisms. Nat. Protoc 2012, 7, 24–35.

(53). Pilkington EH; Gurzov EN; Kakinen A; Litwak SA; Stanley WJ; Davis TP; Ke PC, Pancreatic Beta-Cell Membrane Fluidity and Toxicity Induced by Human Islet Amyloid Polypeptide Species. Sci. Rep 2016, 6, 21274. [PubMed: 26880502]

(54). Peng S; Ding F; Urbanc B; Buldyrev SV; Cruz L; Stanley HE; Dokholyan NV, Discrete Molecular Dynamics Simulations of Peptide Aggregation. Phys. Rev. E 2004, 69, 041908.

(55). Faridi A; Sun Y; Okazaki Y; Peng G; Gao J; Kakinen A; Faridi P; Zhao M; Javed I; Purcell AW; Davis TP; Lin S; Oda R; Ding F; Ke PC, Mitigating Human Iapp Amyloidogenesis in Vivo with Chiral Silica Nanoribbons. Small 2018, 14, 1802825.

(56). Bunce SJ; Wang Y; Stewart KL; Ashcroft AE; Radford SE; Hall CK; Wilson AJ, Molecular Insights into the Surface-Catalyzed Secondary Nucleation of Amyloid-B40 (Aβ40) by the Peptide Fragment Aβ16–22. Sci. Adv 2019, 5, eaav8216.

(57). Yin S; Ding F; Dokholyan NV, Eris: An Automated Estimator of Protein Stability. Nat. Methods 2007, 4, 466–467. [PubMed: 17538626]

(58). Yin S; Biedermannova L; Vondrasek J; Dokholyan NV, Medusascore: An Accurate Force Field-Based Scoring Function for Virtual Drug Screening. J. Chem. Inf. Model 2008, 48, 1656–1662. [PubMed: 18672869]

(59). Brooks BR; Bruccoleri RE; Olafson BD; States DJ; Swaminathan S; Karplus M, Charmm: A Program for Macromolecular Energy, Minimization, and Dynamics Calculations. J. Comput. Chem 1983, 4, 187–217.

(60). Lazaridis T; Karplus M, Effective Energy Functions for Protein Structure Prediction. Curr. Opin. Struct. Biol 2000, 10, 139–145. [PubMed: 10753811]

(61). Ding F; Borreguero JM; Buldyrey SV; Stanley HE; Dokholyan NV, Mechanism for the A-Helix to β-Hairpin Transition. Proteins 2003, 53, 220–228. [PubMed: 14517973]

(62). Gu Z; Plant LD; Meng XY; Perez-Aguilar JM; Wang Z; Dong M; Logothetis DE; Zhou R, Exploring the Nanotoxicology of MoS2: A Study on the Interaction of MoS2 Nanoflakes and K+ Channels. ACS Nano 2018, 12, 705–717. [PubMed: 29236481]

(63). Gu Z; De Luna P; Yang Z; Zhou R, Structural Influence of Proteins Upon Adsorption to MoS2 Nanomaterials: Comparison of MoS2 Force Field Parameters. Phys. Chem. Chem. Phys 2017, 19, 3039–3045. [PubMed: 28079199]

(64). Kabsch W; Sander C, Dictionary of Protein Secondary Structure: Pattern Recognition of Hydrogen-Bonded and Geometrical Features. Biopolymers 1983, 22, 2577–2637. [PubMed: 6667333]

(65). Nguyen PH; Ramamoorthy A; Sahoo BR; Zheng J; Faller P; Straub JE; Dominguez L; Shea JE; Dokholyan NV; De Simone A; Ma B; Nussinov R; Najafi S; Ngo ST; Loquet A; Chiricotto M; Ganguly P; McCarty J; Li MS; Hall C; Wang Y; Miller Y; Melchionna S; Habenstein B; Timr S; Chen J; Hnath B; Strodel B; Kayed R; Lesné S; Wei G; Sterpone F; Doig AJ; Derreumaux P, Amyloid Oligomers: A Joint Experimental/Computational Perspective on Alzheimer's Disease,

Parkinson's Disease, Type Ii Diabetes, and Amyotrophic Lateral Sclerosis. Chem. Rev 2021, 121, 2545–2647. [PubMed: 33543942]

(66). Lin Y; Sahoo BR; Ozawa D; Kinoshita M; Kang J; Lim MH; Okumura M; Huh YH; Moon E; Jang JH; Lee HJ; Ryu KY; Ham S; Won HS; Ryu KS; Sugiki T; Bang JK; Hoe HS; Fujiwara T; Ramamoorthy A; Lee YH, Diverse Structural Conversion and Aggregation Pathways of Alzheimer's Amyloid-β (1–40). ACS Nano 2019, 13, 8766–8783. [PubMed: 31310506]

(67). Sahoo BR; Cox SJ; Ramamoorthy A, High-Resolution Probing of Early Events in Amyloid-Beta Aggregation Related to Alzheimer's Disease. Chem. Commun 2020, 56, 4627–4639.

(68). Kotler SA; Brender JR; Vivekanandan S; Suzuki Y; Yamamoto K; Monette M; Krishnamoorthy J; Walsh P; Cauble M; Holl MM; Marsh EN; Ramamoorthy A, High-Resolution Nmr Characterization of Low Abundance Oligomers of Amyloid-β without Purification. Sci. Rep 2015, 5, 11811. [PubMed: 26138908]

(69). Suzuki Y; Brender JR; Soper MT; Krishnamoorthy J; Zhou Y; Ruotolo BT; Kotov NA; Ramamoorthy A; Marsh EN, Resolution of Oligomeric Species During the Aggregation of Aβ1–40 Using (19)F Nmr. Biochemistry 2013, 52, 1903–1912. [PubMed: 23445400]

(70). Sahoo BR; Genjo T; Bekier M; Cox SJ; Stoddard AK; Ivanova M; Yasuhara K; Fierke CA; Wang Y; Ramamoorthy A, Alzheimer's Amyloid-Beta Intermediates Generated Using Polymer-Nanodiscs. Chem. Commun. (Camb.) 2018, 54, 12883–12886. [PubMed: 30379172]

(71). Sarkar B; Mithu VS; Chandra B; Mandal A; Chandrakesan M; Bhowmik D; Madhu PK; Maiti S, Significant Structural Differences between Transient Amyloid-β Oligomers and Less-Toxic Fibrils in Regions Known to Harbor Familial Alzheimer's Mutations. Angew. Chem. Int. Ed. Engl 2014, 53, 6888–6892. [PubMed: 24756858]

(72). Lee SJ; Nam E; Lee HJ; Savelieff MG; Lim MH, Towards an Understanding of Amyloid-β Oligomers: Characterization, Toxicity Mechanisms, and Inhibitors. Chem. Soc. Rev 2017, 46, 310–323. [PubMed: 27878186]

(73). Lee J; Culyba EK; Powers ET; Kelly JW, Amyloid-β Forms Fibrils by Nucleated Conformational Conversion of Oligomers. Nat. Chem. Biol 2011, 7, 602–609. [PubMed: 21804535]

(74). Barnes CA; Robertson AJ; Louis JM; Anfinrud P; Bax A, Observation of β-Amyloid Peptide Oligomerization by Pressure-Jump Nmr Spectroscopy. J. Am. Chem. Soc 2019, 141, 13762–13766. [PubMed: 31432672]

(75). Österlund N; Moons R; Ilag LL; Sobott F; Gräslund A, Native Ion Mobility-Mass Spectrometry Reveals the Formation of β-Barrel Shaped Amyloid-β Hexamers in a Membrane-Mimicking Environment. J. Am. Chem. Soc 2019, 141, 10440–10450. [PubMed: 31141355]

(76). Serra-Batiste M; Ninot-Pedrosa M; Bayoumi M; Gairí M; Maglia G; Carulla N, Aβ42 Assembles into Specific β-Barrel Pore-Forming Oligomers in Membrane-Mimicking Environments. Proc. Natl. Acad. Sci. U.S.A 2016, 113, 10866–10871. [PubMed: 27621459]

(77). Sun Y; Kakinen A; Wan X; Moriarty N; Hunt CPJ; Li Y; Andrikopoulos N; Nandakumar A; Davis TP; Parish CL; Song Y; Ke PC; Ding F, Spontaneous Formation of β-Sheet Nano-Barrels During the Early Aggregation of Alzheimer's Amyloid Beta. Nano Today 2021, 38.

(78). Yang H; Yang S; Kong J; Dong A; Yu S, Obtaining Information About Protein Secondary Structures in Aqueous Solution Using Fourier Transform Ir Spectroscopy. Nat. Protoc 2015, 10, 382–396. [PubMed: 25654756]

(79). Hong S; Ostaszewski BL; Yang T; O'Malley TT; Jin M; Yanagisawa K; Li S; Bartels T; Selkoe DJ, Soluble Abeta Oligomers Are Rapidly Sequestered from Brain Isf in Vivo and Bind Gm1 Ganglioside on Cellular Membranes. Neuron 2014, 82, 308–319. [PubMed: 24685176]

(80). Meker S; Chin H; Sut TN; Cho NJ, Amyloid-β Peptide Triggers Membrane Remodeling in Supported Lipid Bilayers Depending on Their Hydrophobic Thickness. Langmuir 2018, 34, 9548–9560. [PubMed: 30021071]

(81). Korshavn KJ; Satriano C; Lin Y; Zhang R; Dulchavsky M; Bhunia A; Ivanova MI; Lee YH; La Rosa C; Lim MH; Ramamoorthy A, Reduced Lipid Bilayer Thickness Regulates the Aggregation and Cytotoxicity of Amyloid-Beta. J. Biol. Chem 2017, 292, 4638–4650. [PubMed: 28154182]

(82). Bode DC; Baker MD; Viles JH, Ion Channel Formation by Amyloid-B42 Oligomers but Not Amyloid-B40 in Cellular Membranes. J. Biol. Chem 2017, 292, 1404–1413. [PubMed: 27927987]

(83). O'Brien EP; Straub JE; Brooks BR; Thirumalai D, Influence of Nanoparticle Size and Shape on Oligomer Formation of an Amyloidogenic Peptide. J. Phys. Chem. Lett 2011, 2, 1171–1177. [PubMed: 21691423]

(84). John T; Gladytz A; Kubeil C; Martin LL; Risselada HJ; Abel B, Impact of Nanoparticles on Amyloid Peptide and Protein Aggregation: A Review with a Focus on Gold Nanoparticles. Nanoscale 2018, 10, 20894–20913. [PubMed: 30225490]

(85). Appel JH; Li DO; Podlevsky JD; Debnath A; Green AA; Wang QH; Chae J, Low Cytotoxicity and Genotoxicity of Two-Dimensional MoS2 and Ws2. ACS Biomater. Sci. Eng 2016, 2, 361–367.

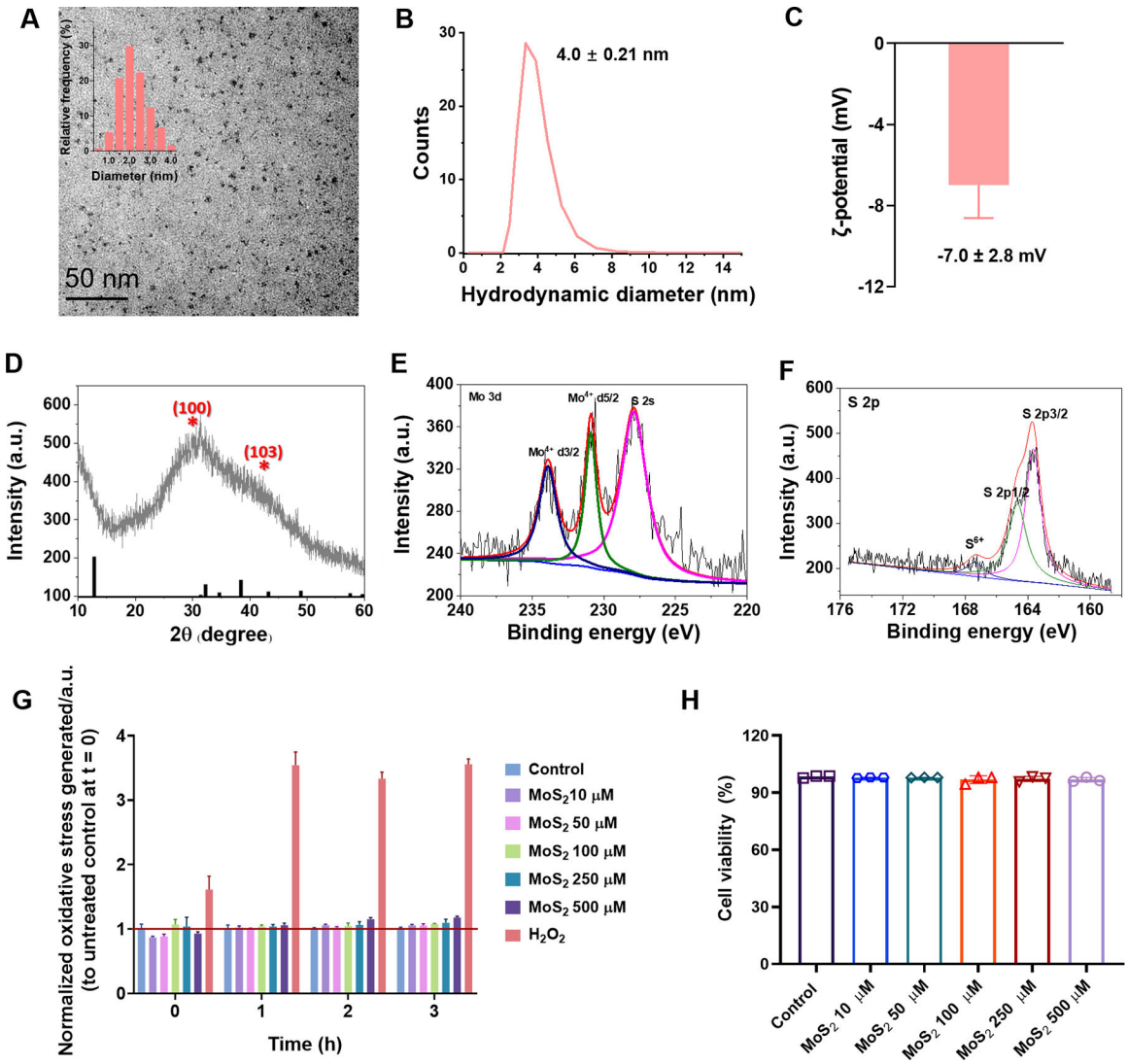

Figure 1. Characterizations of ultrasmall MoS_2 QDs.

(A) TEM imaging of ultrasmall MoS_2 QDs and their corresponding diameter distribution (inset). (B, C) Hydrodynamic diameter and ζ-potential measurement of the ultrasmall MoS_2 QDs. (D) XRD detection of the ultrasmall MoS_2 QDs. (E, F) The Mo 3d, S 2s, and S 2p regions of the XPS spectrum for the ultrasmall MoS_2 QDs. (G) ROS measurements over a time course of 0 h to 3 h and (H) 24 h cell viability for different concentrations of the ultrasmall MoS_2 QDs at SH-SY5Y cells. Data are shown as the mean (n=3) ± SEM and statistical analysis was performed through two-tailed Student's *t*-test. Compared with control, there was no significant difference observed in the ultrasmall MoS_2 QDs.

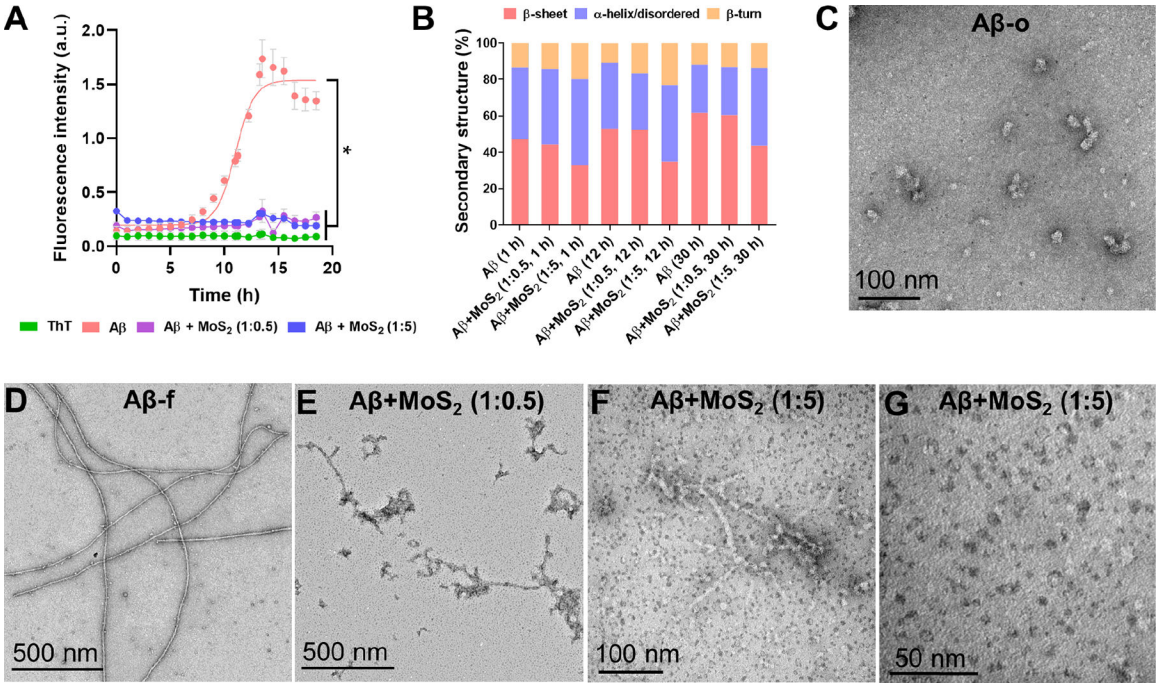

Figure 2. Inhibitory effects of ultrasmall MoS_2 quantum dots on Aβ.

(A) Aβ (50 μM) aggregation in the presence and absence of ultrasmall MoS_2 QDs at the molar ratio of 1:0.5 and 1:5 (Aβ/MoS_2 QDs), monitored by a ThT fluorescence kinetic assay. ThT (100 μM) was used as control and data points were depicted as mean values of repeated measurements (n=3) ± standard errors of the mean (SEM) via two-tailed Student's *t*-test analyzed at 18 h timepoint, *compared with Aβ, $P < 0.05$. (B) Secondary structure distribution of incubated (1, 12 and 30 h) Aβ 50 μM in the presence and absence of ultrasmall MoS_2 QDs. Secondary structure analysis (%) was derived after deconvolution of the respective ATR-FTIR raw spectra presented in Figures S5&S6. (C-G) TEM imaging of Aβ aggregation in the presence and absence of ultrasmall MoS_2 QDs. Aβ concentration: 50 μM. Incubation: 12 h for panel C and 30 h for panels D-G.

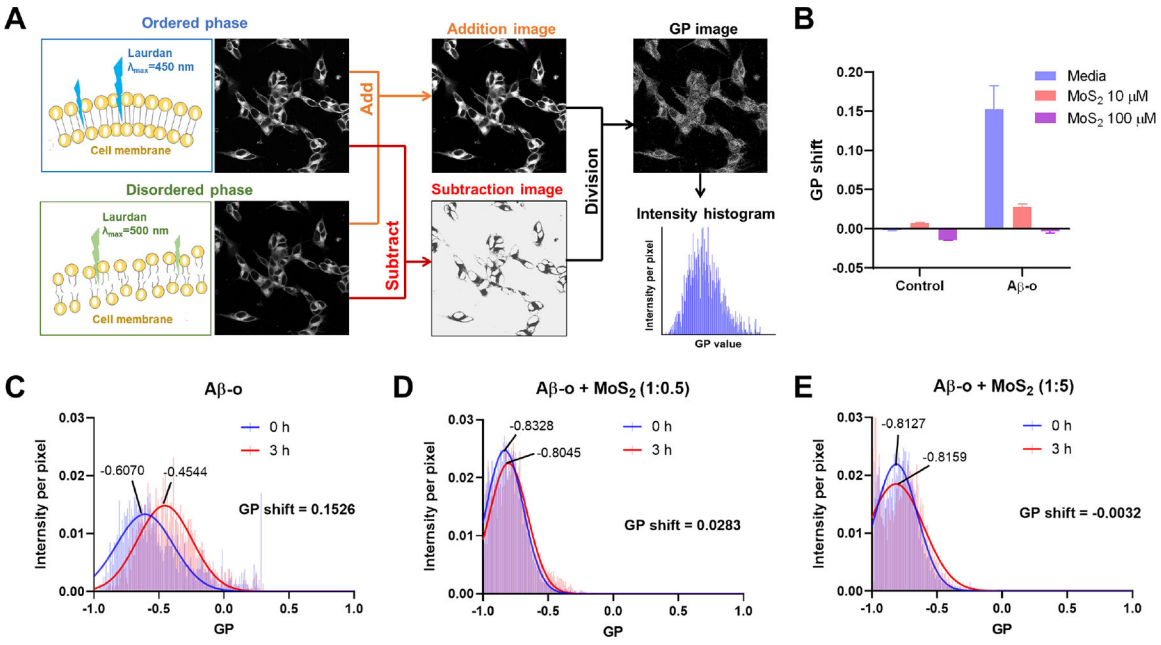

Figure 3. Effect of Aβ oligomers on the fluidity of SH-SY5Y cell membranes in the presence and absence of ultrasmall MoS_2 QDs.

(A) A flowchart illustrates calculation of generalized polarization (GP) values from raw ratiometric confocal images in the ordered and disordered phases. The lipid order of cell membranes was indicated by the lipophilic Laurdan dye, which could partition into cell membranes. When the cell membrane was in the liquid ordered phase, Laurdan dye emitted fluorescence at 450 nm under the excitation of 405 nm, and redshifted to 500 nm when the cell membrane was in the liquid disordered phase. GP images and the pixels of cell membranes were derived with ImageJ software. Intensity shifts between the ordered and disordered channels were quantified as GP values. (B) GP shifts were recorded after a 3 h-treatment by Aβ-o (20 μM) in the presence and absence of ultrasmall MoS_2 QDs (10 or 100 μM). Ultrasmall MoS_2 QDs themselves did not affect cell membrane fluidity in 3 h. (C) Compared to Aβ monomers (Aβ-m) and amyloid fibrils (Aβ-f, Figure S8), Aβ-o are predicted to cause lipid order, and a corresponding positive GP shift. (D, E) MoS_2 could significantly prevent damage to cell membrane fluidity caused by Aβ-o and restore the GP values to control cell level at the higher concentration of 100 μM MoS_2 QDs.

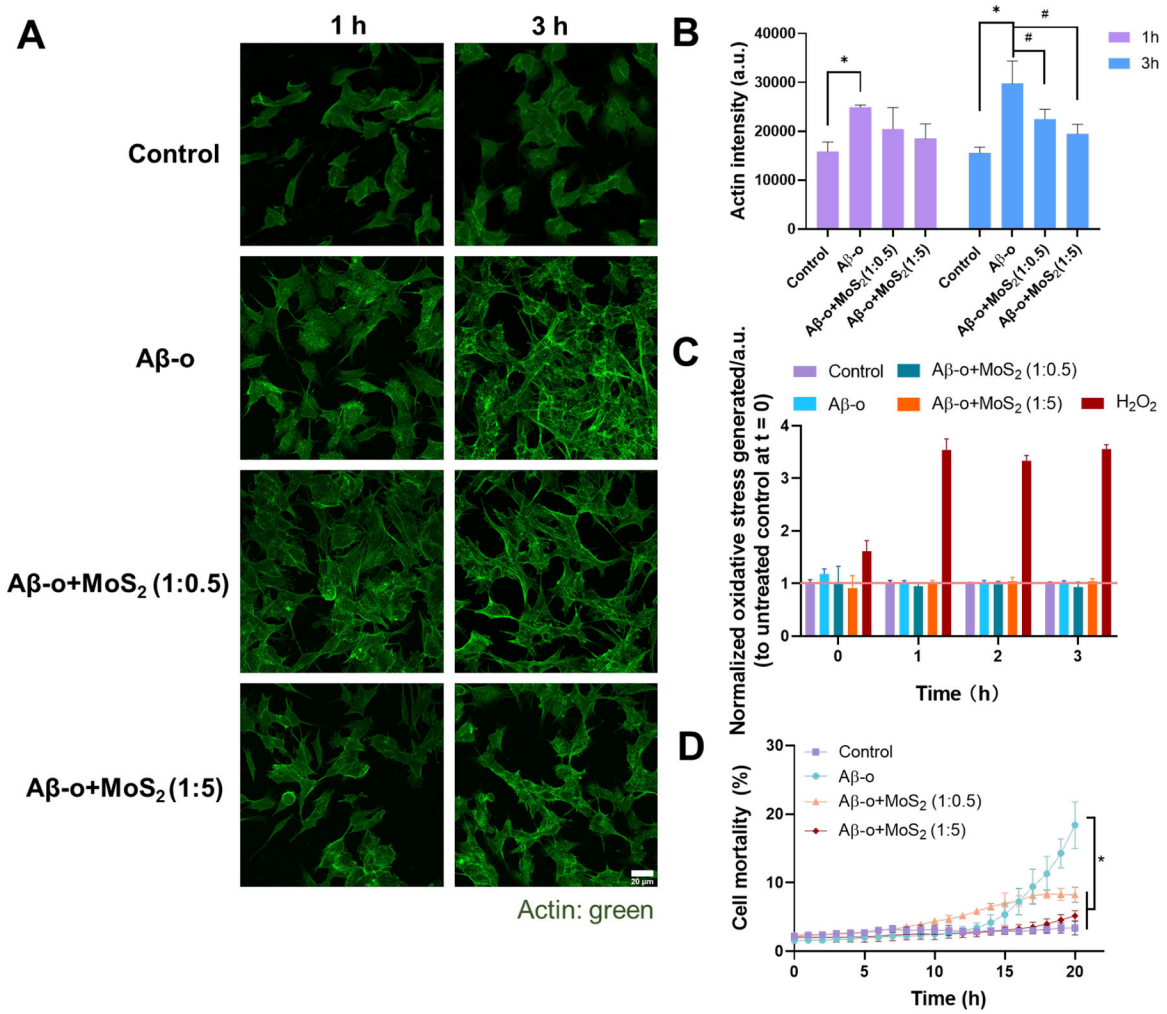

Figure 4. Actin organization, ROS generation and cell viability detection at SH-SY5Y cells after exposure to Aβ-o (20 μM) in the presence and absence of ultrasmall MoS_2 QDs with the molar ratios of 1:0.5 and 1:5.

(A) Immunofluorescence imaging of actin filaments after 1 and 3 h treatment of Aβ-o (20 μM) and ultrasmall MoS_2 QDs (10 and 100 μM). Actin filaments were stained by the phalloidin-iFluor 488 (green). Scale bar: 20 μm. (B) The calculation of actin filaments intensity according to panel A. Data points are depicted as mean values (n=3) ± SEM, via two-tailed Student's t-test, *P < 0.05 compared with control group, #P < 0.05 compared with Aβ-o. (C) ROS production of SH-SY5Y cells were identified by H_2DCFDA staining after 3 h treatment with Aβ-o and the combination of ultrasmall MoS_2 QDs. H_2O_2 (200 μM) was used as positive control. (D) Cell viability after 20 h treatment with Aβ-o and the combination of ultrasmall MoS_2 QDs. Data are shown as mean values (n=3) ± SEM, via two-tailed Student's *t*-test analyzed at 20 h, *compared with Aβ-o, $P < 0.05$.

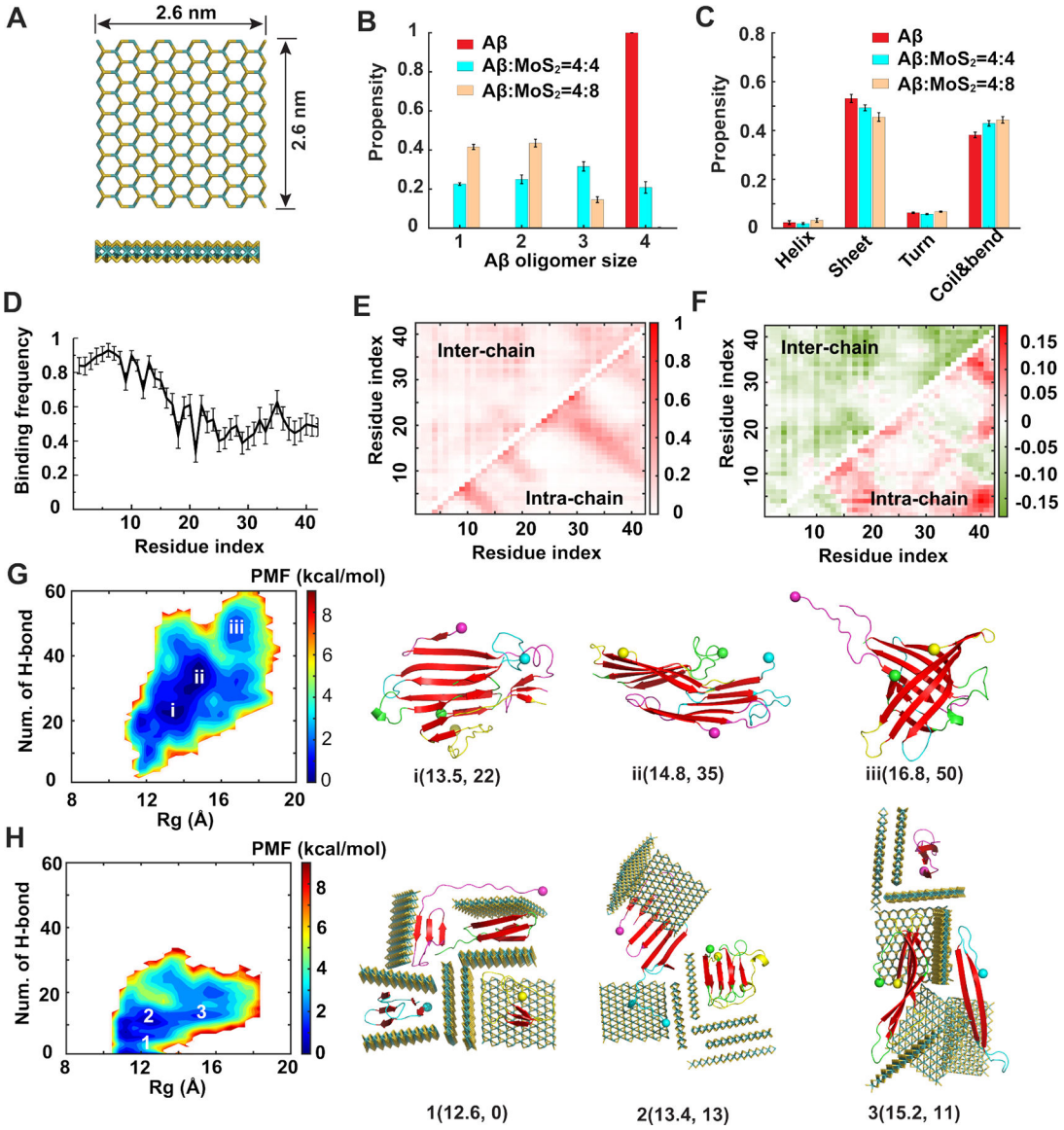

Figure 5. Coaggregation of Aβ peptides with ultrasmall MoS_2 quantum dots.

(A) Atomic structure of the ultrasmall MoS_2 QD used in our simulations. (B) Distribution of Aβ oligomer size in the absence and presence of ultrasmall MoS_2 QDs. (C) Secondary structure propensities of Aβ after the simulations reached the steady state. (D) Binding frequency of each Aβ residue with ultrasmall MoS_2 QDs. (E) Intra- and inter-peptide contact frequency maps for Aβ peptides. (F) Changes of the contact frequency maps for the system with Aβ:MoS_2=4:8 compared with the control one. (G, H) Two-dimensional potential of mean force (PMF) with respect of the number of inter-peptide hydrogen bond (H-bond) and radius of gyration (R_g) for Aβ peptides (G) and Aβ:MoS_2=4:8 (H). The basins of the PMF (i, ii and iii in panel G and 1, 2 and 3 in panel H) were labeled with the typical snapshots presented on the right. Ultrasmall MoS_2 QDs are shown as sticks and colored by elements. Aβ peptides are shown as cartoons and colored by chains with N-termini indicated by spheres and β-sheet structures highlighted in red.

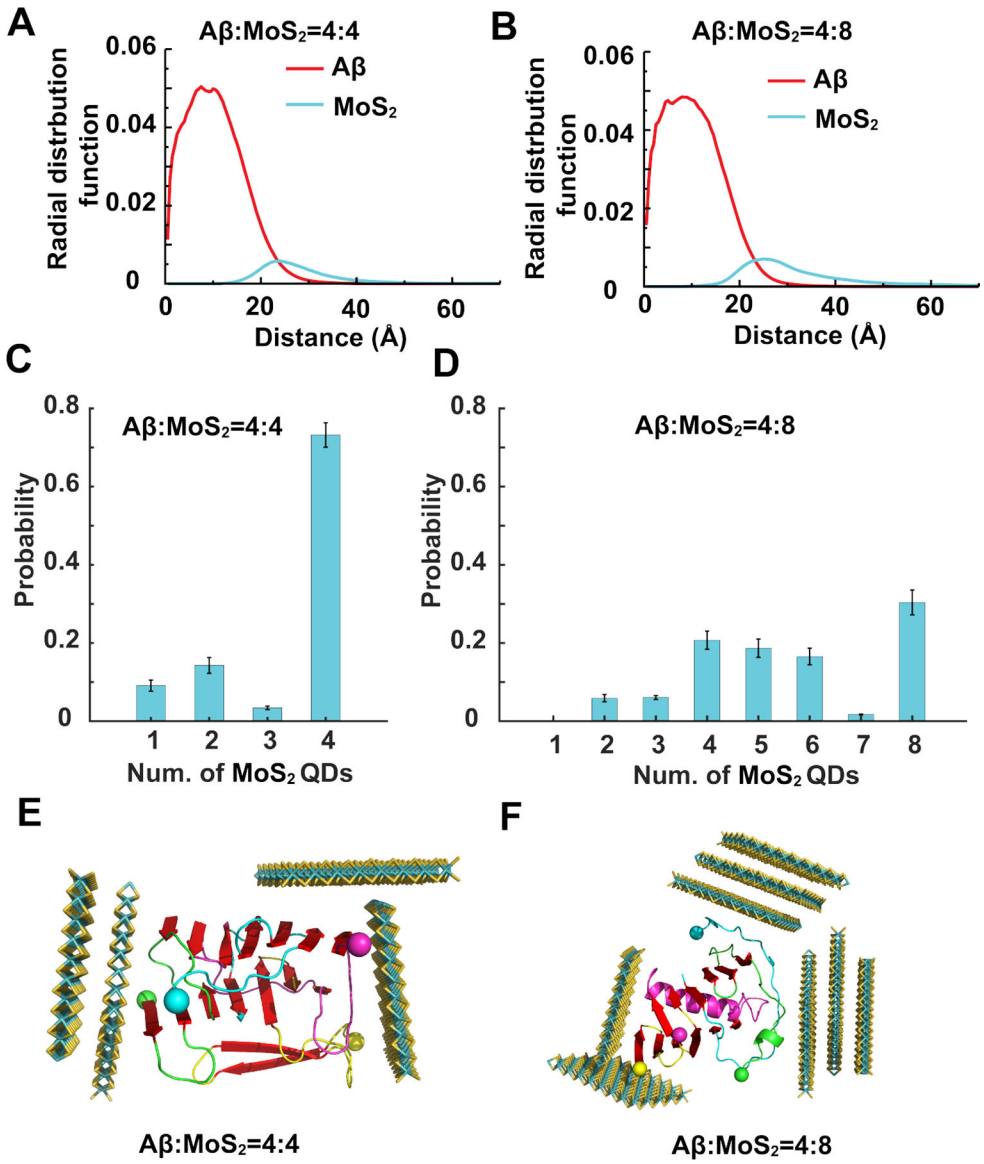

Figure 6. Interactions of ultrasmall MoS_2 quantum dots with Aβ oligomers.

Ultrasmall MoS_2 QDs were added to preformed Aβ tetramers with molar ratios Aβ:MoS_2=4:4 (A, C, E) and Aβ:MoS_2=4:8 (B, D, F). (A, B) Radial distribution functions of Aβ and MoS_2 atoms from the center of mass of the cluster. (C, D) Number of ultrasmall MoS_2 QDs bound on Aβ tetramers after simulations reached steady state. (E, F) Typical testudo-like Aβ-o-MoS_2 complex formations, where ultrasmall MoS_2 QDs in the exterior shielded Aβ-o in the interior. Ultrasmall MoS_2 QDs are shown as sticks and colored by elements. Aβ peptides are shown as cartoons and colored by chains with N-termini indicated by spheres and β-sheet structures highlighted in red.

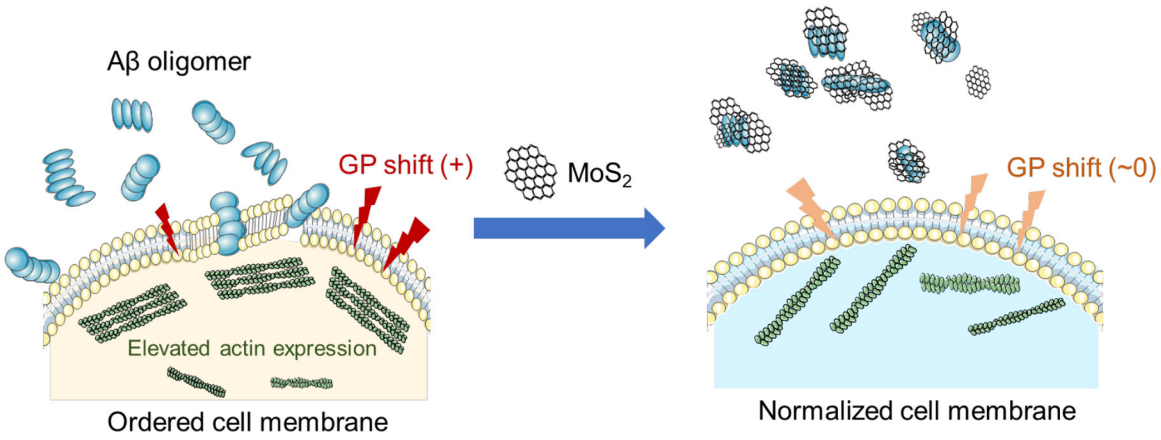

Figure 7. Cell membrane disruption by Aβ oligomers (left) and its rescue by ultrasmall MoS_2 quantum dots (right).

While Aβ-o perturbed membrane integrity (left), association of ultrasmall MoS_2 QDs and Aβ-o depleted the toxic peptide species in the extracellular space from amyloid aggregation and membrane partitioning, and subsequently prevented elevated actin expression in the cytoskeleton. This facile membrane-centric strategy may prove beneficial for future development of multifunctional AD nanomedicines.